UNIVERSITY OF AMSTERDAM

UvA-DARE (Digital Academic Repository)

Discovery of X-ray polarization angle rotation in the jet from blazar Mrk 421

Di Gesu, L.; Ng, C-Y; Vink, J.; IXPE

DOI
10.1038/s41550-023-02032-7

Publication date
2023

Document Version
Final published version

Published in
Nature Astronomy

License
Article 25fa Dutch Copyright Act (https://www.openaccess.nl/en/policies/open-access-in-dutch-copyright-law-taverne-amendment)

Link to publication

Citation for published version (APA):
Di Gesu, L., Ng, C.-Y., Vink, J., & IXPE (2023). Discovery of X-ray polarization angle rotation in the jet from blazar Mrk 421. *Nature Astronomy*, *7*(10), 1245-1258. https://doi.org/10.1038/s41550-023-02032-7

General rights
It is not permitted to download or to forward/distribute the text or part of it without the consent of the author(s) and/or copyright holder(s), other than for strictly personal, individual use, unless the work is under an open content license (like Creative Commons).

Disclaimer/Complaints regulations
If you believe that digital publication of certain material infringes any of your rights or (privacy) interests, please let the Library know, stating your reasons. In case of a legitimate complaint, the Library will make the material inaccessible and/or remove it from the website. Please Ask the Library: https://uba.uva.nl/en/contact, or a letter to: Library of the University of Amsterdam, Secretariat, P.O. Box 19185, 1000 GD Amsterdam, The Netherlands. You will be contacted as soon as possible.

UvA-DARE is a service provided by the library of the University of Amsterdam (https://dare.uva.nl)

Download date:07 Oct 2026

nature astronomy

Article

https://doi.org/10.1038/s41550-023-02032-7

Discovery of X-ray polarization angle rotation in the jet from blazar Mrk 421

Received: 22 February 2023

Accepted: 12 June 2023

Published online: 17 July 2023

Check for updates

A list of authors and their affiliations appears at the end of the paper

The magnetic-field conditions in astrophysical relativistic jets can be probed by multiwavelength polarimetry, which has been recently extended to X-rays. For example, one can track how the magnetic field changes in the flow of the radiating particles by observing rotations of the electric vector position angle Ψ. Here we report the discovery of a Ψ_X rotation in the X-ray band in the blazar Markarian 421 at an average flux state. Across the 5 days of Imaging X-ray Polarimetry Explorer observations on 4–6 and 7–9 June 2022, Ψ_X rotated in total by ≥360°. Over the two respective date ranges, we find constant, within uncertainties, rotation rates (80 ± 9° per day and 91 ± 8° per day) and polarization degrees (Π_X = 10% ± 1%). Simulations of a random walk of the polarization vector indicate that it is unlikely that such rotation(s) are produced by a stochastic process. The X-ray-emitting site does not completely overlap the radio, infrared and optical emission sites, as no similar rotation of Ψ was observed in quasi-simultaneous data at longer wavelengths. We propose that the observed rotation was caused by a helical magnetic structure in the jet, illuminated in the X-rays by a localized shock propagating along this helix. The optically emitting region probably lies in a sheath surrounding an inner spine where the X-ray radiation is released.

Despite decades of effort, the physical processes shaping the dynamics and emission of relativistic jets are in large part still unclear (for example, ref. 1). However, in the past decade, several important clues have been obtained owing to new facilities that allow the possibility of following in detail the time-variable emission properties of jets, especially at high photon energies. A similar leap is now expected from the newly opened window of X-ray polarimetry, which provides us with an unprecedented view of the physical sites of particle acceleration and emission.

Blazars, whose relativistic jets point close to Earth, provide excellent laboratories to investigate the physics of jets and test current theoretical ideas (for example, ref. 2). Among blazars, the so-called high-peaked BL Lacertae objects (HBLs), whose synchrotron and Compton components peak in the X-ray and very-high-energy γ-ray band, respectively, are the ideal sources to investigate acceleration and cooling processes acting on ultrarelativistic electrons (with Lorentz factors $\gamma \gtrsim 10^6$). From the theoretical point of view, the main mechanisms advocated for the energization of particles in relativistic jets are diffusive shock acceleration (for example, ref. 3), magnetic reconnection (for example, ref. 4), possibly triggered by instabilities (for example, ref. 5) or specific anti-parallel magnetic-field structures[6], or reconnection plus stochastic acceleration in relativistic turbulence in a highly magnetized plasma (for example, ref. 7).

Polarimetry is a powerful tool that can break the degeneracies involved in the modelling of the spectral energy distribution (SED) and gain insight into the magnetic-field and emission-region geometry[8]. Recent theoretical efforts have allowed us to identify polarimetric signatures expected under different scenarios of blazar emission regions that can be contrasted with observational evidence. Polarimetric measurements are sensitive to the geometrical structure of the magnetic field permeating the flow and to its global properties (for example, chaotic versus globally ordered). In particular, the evidence for systematic and large variations of the polarization angle, potentially associated with powerful γ-ray flares (for example, refs. 9,10), has been interpreted in terms of a helically twisted jet (for example, ref. 11), an emission region moving along helical field lines that propagate down the jet (for example, refs. 12–14), or light-travel delays when a shock forms in

e-mail: laura.digesu@asi.it

https://doi.org/10.1038/s41550-023-02032-7

Table 1 | Log of polarization measurements of Mrk 421 used in this work

Telescope	Band (eV)	Dates (YYY-MM-DD)	Radio flux density (10^{-25} erg s^{-1} cm^{-2} Hz^{-1})	Radio polarization	
				Π_R (%)	Ψ_R (°)
SMA	9.5×10^{-4}	2022-06-04	28±2	2.3±0.2	130±2
SMA	9.5×10^{-4}	2022-06-16	38±2	2.3±0.2	133±4
IRAM	3.5×10^{-4}	2022-05-04	28±1	3.0±0.7	237±7
IRAM	3.5×10^{-4}	2022-05-05	38±2	3.8±0.7	232±4
IRAM	3.5×10^{-4}	2022-05-31	32±2	7.9±0.8	128±2
IRAM	3.5×10^{-4}	2022-05-06	36±1	1.8±0.6	116±9
VLBA	1.7×10^{-4}	2022-04-30	34.6±0.1	1.6±0.3	100±10
VLBA	1.7×10^{-4}	2022-06-05	27.6±0.1	2.6±0.3	147±10
VLBA	1.7×10^{-4}	2022-06-24	25.6±0.1	2.2±0.3	132±10

Telescope	Band (eV)	Dates (YYY-MM-DD)	Infrared flux density (10^{-25} erg s^{-1} cm^{-2} Hz^{-1})	Infrared polarization	
				Π_{IR} (%)	Ψ_{IR} (°)
Perkins	H:0.9	2022-05-04	3.92±0.05	1.3±0.5	220±11
Perkins	H:0.9	2022-05-05	1.77±0.03	2.9±0.8	212±8
Perkins	H:0.9	2022-05-09	4.19±0.05	3.1±0.8	181±7
Perkins	H:0.9	2022-05-14	3.55±0.04	1.7±1.0	175±17
Perkins	H:0.9	2022-06-06	4.87±0.05	3.9±0.5	128±3
Perkins	H:0.9	2022-06-07	4.52±0.05	4.8±0.9	147±5
Perkins	H:0.9	2022-06-08	4.14±0.06	6.2±1.3	145±6
Kanata[a]	H:0.9	2022-05-04	–	3.1±0.2	197±2
Kanata[a]	H:0.9	2022-05-05	–	3.4±0.3	187±4

Telescope	Band (eV)	Dates (YYYY-MM-DD)	Optical flux density (10^{-25} erg s^{-1} cm^{-2} Hz^{-1})	Optical polarization	
				Π_O (%)	Ψ_O (°)
Skinakas	R:1.9	2022-05-13	1.60±0.04	2.7±0.2	192±2
Skinakas	R:1.9	2022-05-13	1.64±0.04	3.2±0.2	195±2
Skinakas	R:1.9	2022-05-13	1.61±0.04	2.7±0.2	193±2
Skinakas	R:1.9	2022-05-14	1.48±0.04	3.7±0.2	179±2
Skinakas	R:1.9	2022-05-16	1.41±0.04	3.5±0.3	176±2
Skinakas	R:1.9	2022-05-18	1.41±0.04	2.7±0.4	179±5
Skinakas	R:1.9	2022-05-22	1.53±0.04	3.3±0.2	118±2
Skinakas	R:1.9	2022-05-30	2.02±0.04	5.6±0.2	149±1
Skinakas	R:1.9	2022-05-31	1.98±0.04	5.4±0.2	150±1
Skinakas	R:1.9	2022-06-01	2.05±0.04	5.3±0.2	142±1
Skinakas	R:1.9	2022-06-02	1.93±0.04	5.1±0.2	152±1
Skinakas	R:1.9	2022-06-07	2.12±0.04	5.4±0.3	145±1
Skinakas	R:1.9	2022-06-17	2.05±0.04	4.7±0.3	152±2
NOT	R:1.9	2022-05-04	1.89±0.04	2.9±0.1	202±1
NOT	R:1.9	2022-06-04	2.02±0.04	4.8±0.1	153±1
NOT	R:1.9	2022-06-05	2.25±0.04	3.9±0.1	133±1
NOT	R:1.9	2022-06-06	2.27±0.07	5.6±0.2	146±1
SNO	R:1.9	2022-01-16	2.34±0.01	3.8±0.4	136±3
SNO	R:1.9	2022-04-19	1.95±0.01	4.6±0.7	264±3

Table 1 (continued)| Log of polarization measurements of Mrk 421 used in this work

Telescope	Band (eV)	Dates (YYYY-MM-DD)	Optical flux density (10^{-25} erg s^{-1} cm^{-2} Hz^{-1})	Optical polarization	
				Π_O (%)	Ψ_O (°)
SNO	R:1.9	2022-06-16	2.40±0.50	9.5±1.1	137±4
Kanata[a]	R:1.9	2022-05-04	2.50±0.40	3.1±0.2	200±1
Kanata[a]	R:1.9	2022-05-05	2.20±0.02	3.4±0.3	201±1

Telescope	Energy range (keV)	Dates (YYYY-MM-DD)	X-ray flux (10^{-11} erg s^{-1} cm^{-2})	X-ray polarization[b]	
				Π_X (%)	Ψ_X (°)
IXPE	2.0-8.0	2022-05-04	8.67±0.03	15±2	35±4
IXPE	2.0-8.0	2022-06-04	15.69±0.09	Not detected	
IXPE	2.0-8.0	2022-06-07	30.2±0.2	Not detected	

[a]Not corrected for dilution of polarization by unpolarized starlight from the host galaxy. [b]X-ray polarization degrees are for the time-averaged IXPE data.

a jet with a predominantly helical/toroidal field[15,16]. Such a structure for the global field is supported by (spatially resolved) polarimetric studies of parsec-scale jets in the radio band[17,18]. Interaction between a moving and a stationary shock can also produce large rotations (for example, ref. 19). An alternative explanation is that the polarization behaviour is stochastic, related to turbulence in the flow[20,21], possibly combined with a standing shock[22,23]. In this framework, the observed polarimetric parameters do not carry any direct information on the structure of the magnetic field in the jet, as they are mainly related to the turbulent nature of the flow. Turbulence can play an important role even if an average ordered magnetic field is present. In this case, while the polarization angle can display rotations related to the effect of the ordered field, the overall level of polarization can be decreased by the depolarizing effect of turbulence (for example, refs. 24,25).

Markarian 421 (Mrk 421) is a nearby (redshift $z = 0.0308$) HBL that has been intensively studied at many wavelengths (for example, ref. 26). It is among the first blazars detected at both gigaelectronvolt (by the Energetic Gamma Ray Experiment Telescope onboard the Compton Gamma Ray Observatory[27]) and teraelectronvolt energies (by the Whipple Observatory[28]). It is bright and well monitored in the X-ray band (for example, refs. 29,30), where the synchrotron SED peaks at a high flux level, making it a prime target for linear polarization observations by the Imaging X-ray Polarimetry Explorer (IXPE).

Results

In the first year of IXPE operation, we observed the blazar Mrk 421 three times (on 4 May, 4 June and 7 June 2022) to search for multi-epoch variability of the X-ray polarization properties. In this case, a single IXPE pointing extends over ~2 days, which permits a search for intra-day variations of the polarization properties as well[25]. The IXPE observations were complemented with radio-millimetre (Very Long Baseline Array (VLBA), Institut de Radioastronomie Millimetrique (IRAM) and the SubMillimeter Array (SMA)), infrared (Kanata, Perkins Telescope), and optical polarization measurements (Kanata, Nordic Optical Telescope (NOT), Observatorio de Sierra Nevada (SNO) and Skinakas Observatory), as detailed in Table 1 and shown in Fig. 1. We captured the source in an average activity state relative to its flux history (Methods), discounting occasional major, multi-band outbursts[31].

In May 2022, Mrk 421 was significantly X-ray polarized (with a polarization degree $\Pi_X \approx 15\%$ at a position angle $\Psi_X \approx 35°$) and did not exhibit any substantial variability of the X-ray polarization properties within the IXPE pointing[32]. This is consistent with the X-ray polarization

https://doi.org/10.1038/s41550-023-02032-7

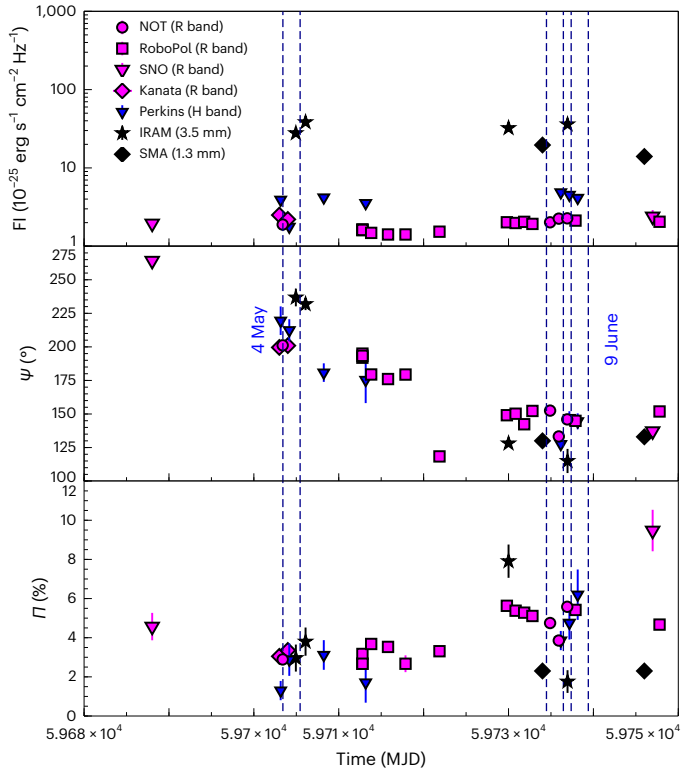

Fig. 1 | Time evolution of the multiwavelength polarization and spectral properties of Mrk 421 in April–June 2022. From top to bottom panel: flux density (FI), polarization angle and polarization degree of Mrk 421 at radio/millimetre (IRAM, black stars; SMA, black diamonds), infrared (Perkins, blue triangles) and optical (NOT, magenta circles; RoboPol, magenta squares; SNO, magenta triangles; Kanata, magenta diamonds) wavelengths as a function of time (Modified Julian Day). The dashed vertical lines mark the beginning and the end of each of the three IXPE observations. Error bars represent a confidence interval of 68%.

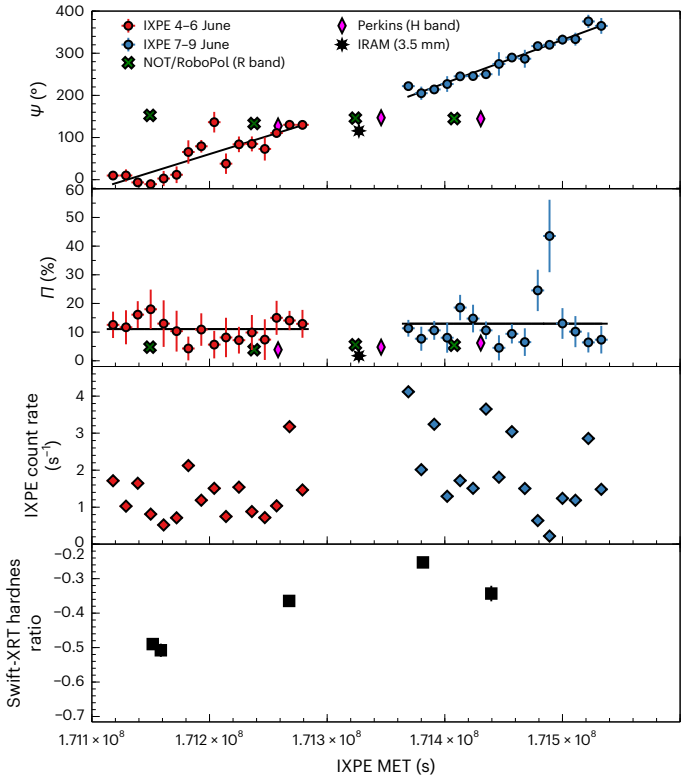

Fig. 2 | Time evolution of the X-ray polarization of spectral properties of Mrk 421 within the IXPE pointings of June 2022. From top to bottom: X-ray polarization angle, degree, IXPE photon count rate and Swift-XRT hardness ratio as a function of time (IXPE MET). MET, mission elapsed time). The IXPE data are in time bins of ~3 h within pointings of 4 June (red diamonds) and 7 June (blue diamonds). Swift-XRT hardness ratios are shown as black squares. As a comparison, we show the polarization properties from simultaneous radio (IRAM, black stars), infrared (Perkins, magenta diamonds) and optical observations (NOT/RoboPol, green crosses). In all the panels, error bars represent a confidence interval of 68%.

of Mrk 501, the other prototypical HBL observed by the IXPE[33]. In both cases, the X-ray polarization degree was larger than at radio, infrared and optical wavelengths. This suggested that the X-rays are produced by rapidly cooling, high-energy electrons accelerated at a shock, while the emission at longer wavelengths is emitted in a larger, downstream region containing a more disordered magnetic field and lower-energy electrons at increased distances from the shock.

In contrast, during two subsequent IXPE observations in June 2022, the X-ray polarization was undetected in the time-averaged IXPE data (Methods). In these observations, the X-ray flux was twice as high as in May 2022 (~1.5×10^{-10} erg s^{-1} cm^{-2} and ~3.02×10^{-10} erg s^{-1} cm^{-2} in the 2–8 keV IXPE band on 4–6 June and 7–9 June, respectively). A similar increase in flux (by a factor of ~1.2; Table 1 and Fig. 1) was also measured in the radio (IRAM), infrared (Perkins) and optical (NOT) data between 4–5 May and 6–7 June 2022.

When measured over shorter time intervals of the IXPE observations of June 2022 (Fig. 2), the X-ray polarization angle varied significantly in a manner consistent with a smooth rotation, as often observed for blazars in the optical band (for example, refs. 34–38). For example, on 4–6 June the X-ray polarization angle Ψ_X varied from 9° ± 1° at the beginning of the IXPE pointing to 130° ± 11° at the end of the observation, while on 7–9 June, Ψ_X changed from 222° ± 7° to 360° ± 20° (considering time bins of ~3 h, as in Fig. 2). We adopt a simple model where the polarization angle rotates at a constant rate, while the polarization degree remains constant, to test the hypothesis that a polarization angle rotation caused cancelling of the polarization degree in the time-averaged data. Using a maximum-likelihood method, a fit of binned Stokes-parameter time series, and a fit in the Q–U plane (where Q and U are the Stokes parameters, see Methods), three independent analyses by subsets of the authors support this hypothesis. The data of 4–6 June are consistent with a rotation rate $\dot{\Psi}_X$ of 80 ± 9° per day at constant Π = 10% ± 1%, while for the data of 7–9 June the parameters are $\dot{\Psi}_X$ = 91 ± 8° per day and Π_X = 10% ± 1%. Our analysis suggests that both Π_X and $\dot{\Psi}_X$ probably varied somewhat with time about the above average values.

While the X-ray polarization angle was rotating, the millimetre-wave, infrared and optical polarization angles did not vary substantially (Fig. 2). In the VLBA images of the radio core of 5 June (Methods), some fanning out of the polarization vectors on the southeast side of the the core is apparent, which indicates an azimuthal component to the magnetic field, as one would expect if that component were helical. In the optical, the scatter of Ψ_0 during the June IXPE observations is ~20°, with no significant trend. Given the gaps in the optical observations, and considering the intrinsic 180° ambiguity, it is possible that a poorly sampled rapid rotation occurred. However, no straightforward scenario makes all the radio, infrared and optical data points consistent with the time series of the X-ray polarization angle. Therefore, we conclude that polarization angle rotation at the longer wavelengths was either absent or proceeded at a different rate compared with the X-ray band.

Simultaneously with the polarization angle rotation, the X-ray spectrum changed significantly (Fig. 2, bottom, and Methods). Swift X-ray Telescope (XRT) data taken over the same time frame as the IXPE pointing show that the flux in the 2.0–10.0 keV band increased by a factor of ~3, while in the 0.3–2.0 band the increase in flux was by a

https://doi.org/10.1038/s41550-023-02032-7

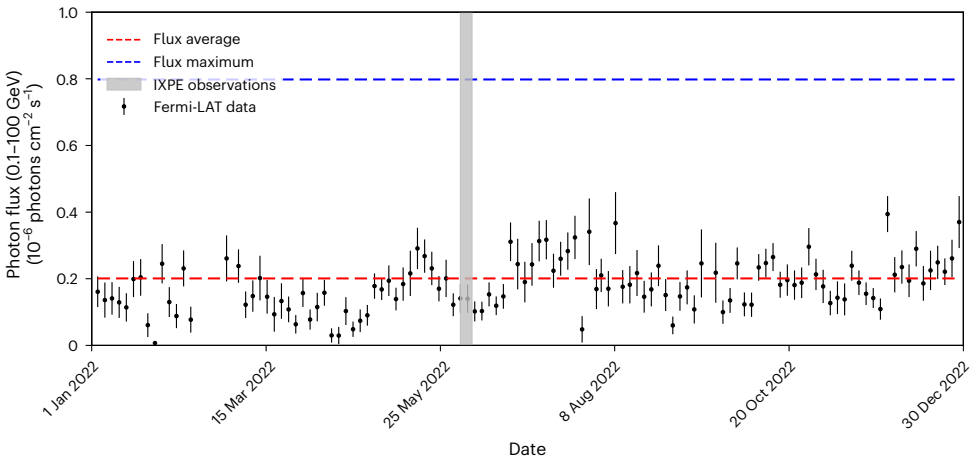

Fig. 3 | Fermi-LAT light curve of Mrk 421. The data are integrated over the 0.1–100 GeV energy range. The grey band marks the time range of the two IXPE observations of Mrk 421 discussed in this work. The red dashed line indicates the average photon flux of Mrk 421 over the LAT mission duration, while the blue solid line marks the highest photon flux recorded by the LAT, which corresponds to the Mrk 421 flare of 2012. The plots include only data points for which the test statistic for source detection is above 9σ. Error bars represent a confidence interval of 68%.

factor of ~1.2. The maximum flux was recorded by the Swift-XRT in correspondence with the beginning of the second IXPE pointing. Then, by the end of the IXPE observation, the source brightness relaxed back to the same level as in the beginning. The spectral shape also changed in a harder-when-brighter fashion, with the brightest point corresponding to the flattest (hardest) spectrum. In contrast, in May 2022, the X-ray flux during the IXPE pointing changed in a similar fashion, but with no change in X-ray spectral shape or polarization angle[32]. At approximately gigaelectronvolt γ-ray energies, Mrk 421 was in a quiescent state during the IXPE pointing: the Fermi Large Area Telescope (LAT)[39] observed minor activity in the 6-month period around the IXPE observations, never reaching more than twice the average catalogue flux (Fig. 3).

Discussion

Virtually all of the processes shaping the dynamics of particles in blazar jets predict specific characteristics of variability of the optical-to-X-ray polarization properties[40], which we can compare against our observations of Mrk 421. Our basic finding conforms to the scenario of an energy-stratified jet, as discussed above for Mrk 421 in May 2022 and for Mrk 501. We find that the roughly constant value of Π_X, while the polarization angle was rotating, is higher than Π_O, Π_{IR} and Π_R, and similar to the level observed at non-rotating epochs. In addition, simultaneous radio, infrared and optical polarization measurements do not show evidence of a similar polarization angle rotation. Due to the limited sampling and intrinsic 180° ambiguity, we cannot exclude the possibility that the optical polarization angle was rotating at some level. However, we consider a rotation of the optical polarization angle at the same rate as the X-ray polarization angle unlikely. Indeed, typical optical polarization rotation rates of blazars vary between a few and a few tens of degrees per day[41], in contrast to the ~85° per day that we estimated in the X-ray. The optical rotation rates may be higher during bright outbursts associated with the passage of knots through the radio core[19,42]. No such outburst was recorded for Mrk 421 at the time of the IXPE pointings. Moreover, no solution of the 180° ambiguity can completely reconcile the radio, optical and infrared polarization angle time series with the X-ray curve. Therefore, as the polarization angle was probably not rotating (or rotating in a different way) at longer wavelengths, we suggest that the radio, infrared and optical emission sites are, at most, only partially co-spatial with the X-ray emission region.

In an energy-stratified jet, the X-rays are emitted closer to the site of acceleration of the particles, while the lower-energy particles emitting at radio-to-optical wavelengths span a larger region downstream owing to their longer radiative cooling times (for example, ref. 33). Acceleration of electrons by a shock can explain the high X-ray polarization, as the shock front partially aligns a previously disordered magnetic field (for example, refs. 43,44). The harder-when-brighter spectral behaviour that Mrk 421 displayed while the X-ray polarization angle was rotating is also expected within the shock scenario[45].

The energy stratification of the particles in the jet can be either linear, in the downstream direction, or radial, in the case of a structured jet[46–48], including an inner fast spine surrounded by a slower sheath. Such a spine-sheath jet explains, for example, the limb-brightening morphology that has been reported in very long-baseline interferometry radio maps of HBLs, including Mrk 421 (refs. 49,50). In the first case, the turbulent component of the magnetic field could become increasingly dominant over the ordered component with distance from the shock[51]. In the second case, turbulence may prevail in the sheath. In both these frameworks, the particle-energy stratification would lead to lower polarization of the optical, infrared and radio emission. Detailed modelling of the variability of flux and polarization induced by turbulence predicts erratic variability, as seen in the past at optical wavelengths in Mrk 421 (ref. 51), which may by chance result in an apparent rotation of the polarization angle[22]. However, such apparent rotations are highly unlikely to explain, for example, the systematic rotations of the optical polarization angle in BL Lacertae and PKS 1510−089 (refs. 34,35). This has led to the proposal that these events occurred upstream of the most turbulent region of the jet. In a larger study of a number of optical-band rotation events in a sample of blazars, it was found that a random walk of the polarization vector cannot reproduce the majority of the observed properties of the population[9,52].

We have investigated whether the rotation of the polarization vector in Mrk 421 could be produced through random walks of the polarization angle by comparing the observations against simulated polarization light curves, following refs. 52,53 (Methods). We consider two scenarios: either the rotations in the observations on 4–6 June and 7–9 June are independent events, or they are part of a single long rotation that spanned seven days, of which we observed two segments separated by a one-day gap. In either scenario, we find, under the most favourable conditions, that only about 2% of the simulated curves of $\dot{\Psi}_X$ and Π_X versus time are consistent with the observations. For the second scenario, if the rotation were actually longer than 7 days, the fraction of simulation trials that reproduce the observed properties would decrease. This suggests that it is unlikely that the observed behaviour can be attributed to random variations of the polarization

https://doi.org/10.1038/s41550-023-02032-7

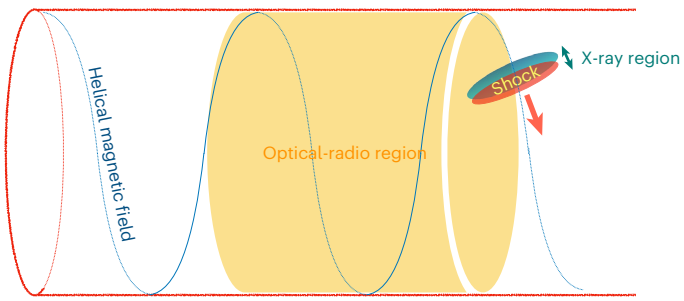

Fig. 4 | Sketch of the scenario proposed to explain the X-ray polarization angle rotation in Mrk 421. In the reference frame of the host galaxy, an off-axis emission feature, for example, a magnetosonic shock, propagates along helical magnetic field lines down the jet.

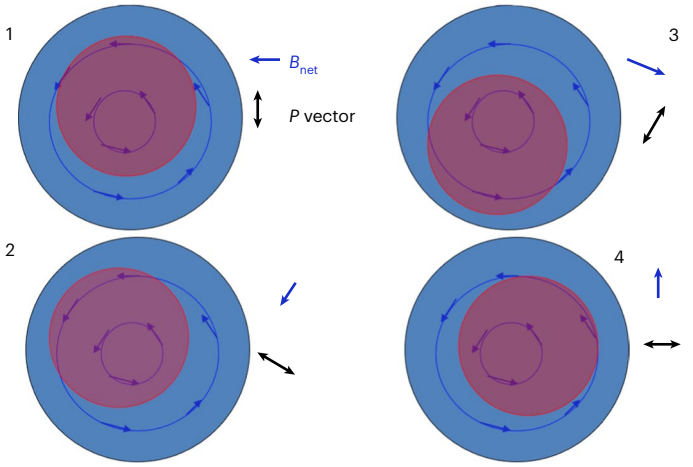

Fig. 5 | Sketch of the scenario proposed to explain the X-ray polarization angle rotation in Mrk 421. We show the appearance of the emission feature, magnetic field (B_{net}) and polarization (P) vector at four azimuthal positions along its spiral path as viewed by a distant observer aligned with the jet. The red circle represents the emission feature and the blue-shaded region is the ambient jet.

angle, and instead points to a coherent, deterministic process responsible for the observed rotation(s).

Magnetic reconnection episodes, which can result from the development of a large-scale kink instability[54] or current sheet[55], may also cause rapid polarization angle swings. These could be associated with γ-ray flares[56] or quasi-periodic oscillations of the source flux[57,58]. In our case, we did not witness any such oscillations or γ-ray flare while the polarization angle was rotating. Moreover, in contrast to our observations of Mrk 421, simulations of magnetic reconnection often display, on average, a similar level of polarization degree in the X-ray and in the optical[25]. In some cases, the X-ray polarization degree can also be much lower than the optical because of time averaging of the polarization vector, which is the opposite of what is observed[25].

A specific model for deterministic polarization angle rotation involves an off-axis emission feature, such as a magnetosonic shock, propagating towards the observer and down a helical magnetic field[11,13,14,16]. The observed rotation rate is determined by the time required for the feature to execute an orbit around the jet axis, modulated by light-travel delays and possibly other relativistic effects[59]. We show sketches of this scenario in Figs. 4 and 5, in the reference frame of the host galaxy and as seen by an observer whose line of sight is along the jet axis, respectively.

As a quantitative example of such a model, we find that we can reproduce the observed rotation rate $\dot{\Psi}_X \approx 85°$ per day over 5 days if (1) the centre of the emission feature is displaced by 2×10^{16}–4×10^{16} cm from the jet axis (for an angle to the line of sight ranging from 4° to 0°), and (2) moves at a velocity of 0.99875c, (i.e. Lorentz factor of 20), with a component parallel to the jet axis of 0.9975c and a transverse, rotational component of 0.05c. c, speed of light. During the rotation, the feature moves through a distance between 0.8 pc and 1.7 pc (depending on the line-of-sight angle) parallel to the line of sight in the observer's frame.

If the jet is structured, the helical field component may be limited to the spine. Moreover, the spine can also contribute somewhat to the emission at longer wavelengths. This would lead to different polarization behaviour in X-ray than at longer wavelengths, and, at the same time, can explain a possible rotation of the optical polarization angle and the similarities in the variability of the X-ray to millimetre fluxes on longer timescales (that is, between May and June 2022).

The discovery of X-ray polarization angle rotation in HBLs, made possible by the new capability of the IXPE, opens up the possibility of fully investigating analogies and differences between polarization angle rotations at different frequencies and for different classes of blazars. For example, ref. 60 discusses a version of the model in which the polarization angle rotations occur immediately downstream of a shock, where the compressed magnetic field is dominated by an ordered (helical) magnetic field superposed on a turbulent component. As the shock is the site of acceleration of the particles that radiate at the frequency of the peak of the synchrotron SED, the highest polarization and main rotation events should be observed near that frequency. This argument has been invoked to explain why optical polarization angle rotations preferably occur in low-synchrotron-peak blazars[61], and naturally predicts a more frequent occurrence of X-ray polarization angle rotations in the case of HBLs. In the same speculative framework, as optical polarization angle rotations are often correlated with approximately gigaelectronvolt γ-ray flares[37], X-ray polarization angle rotations should be accompanied by approximately teraelectronvolt activity, which is, in the case of HBLs, the analogue of approximately gigaelectronvolt activity for low-synchrotron-peak blazars.

In conclusion, this study of the X-ray polarization angle rotation in HBLs in a multiwavelength framework shows how the availability of the X-ray polarization diagnostic enriches our ability to probe the magnetic-field geometry and particle acceleration in different regions of relativistic jets, and thereby represents a fundamental step towards a comprehensive view of relativistic astrophysical jets.

Methods

IXPE and multiwavelength data

IXPE data. The log of all of our observations of Mrk 421 in May–June 2022, including radio/millimetre, optical, infrared and X-ray polarization measurements, along with Swift monitoring in the X-ray band, is listed in Table 1 and Supplementary Table 1.

Here we report the analysis of the second and third IXPE observations of Mrk 421 that were performed from 11:20 UTC on 4 June 2022 to 11:00 UTC on 6 June (hereafter Obs. 2), and from 09:00 UTC on 7 June to 11:10 UTC on 9 June (hereafter Obs. 3). The lifetimes for these pointings are ~96 ks and ~86 ks, respectively.

The raw IXPE data were processed using a standard pipeline (https://heasarc.gsfc.nasa.gov/docs/ixpe/analysis/IXPE-SOC-DOC-009-UserGuide-Software.pdf) that estimates the photo-electron emission direction, correcting for charging effects, detector temperature, gas electron multiplier gain non-uniformity and instrumental spurious modulation[62]. The level-2 event files (one for each of the three detector units onboard IXPE) from the pipeline contain all the information typical of an imaging X-ray astronomy mission (for example, photon arrival time, detector coordinates and energy), with the addition of the polarization information in the form of event-by-event Stokes parameters. Before proceeding with the scientific analysis, when necessary, we adjusted the data for small time-dependent changes to the

gain correction obtained from data taken with the onboard calibration sources close to the actual time of observation[63].

We performed the scientific analysis of the IXPE data using the ixpeobssim software[64,65]. At the angular resolution of IXPE (~30″), blazars like Mrk 421 are point-like sources. Using the xpselect tool, we selected the source events using a circular 60″ radius region, while we used an annulus centred on the source (with inner and outer radii of 2.5′ and 5.0′) to estimate the background. Within the ixpeobssim suite, the method of ref. 66 for estimating the polarization of a set of events is implemented in the PCUBE algorithm. We created the Stokes-parameter spectra of the source, using the PHA1, PHAQ and PHAU algorithms. The PHA1, PHAQ and PHAU algorithms map the I, Q and U Stokes parameters of the photons into OGIP-compliant PHA spectral files (three Stokes-parameter spectra per three detector units). We prepared the spectra for the spectropolarimetric fit by binning the I spectrum, requiring a minimum of 30 counts in each energy bin, as needed for the χ^2 statistics in the fits. Finally, we binned the Q and U spectra by grouping the channels by a constant factor of 10. To search for variability of the flux and polarization properties within the time span of the IXPE pointings, we created light curves with different time binning, using the LC algorithm in ixpeobssim. We applied the time binning of these light curves to time-slice each of the event files and computed a PCUBE in each time interval. We thereby created light curves of the polarization properties as a function of time (t), including normalized Stokes parameters ($q(t)$,$u(t)$), polarization degree ($\Pi(t)$) and polarization angle ($\Psi(t)$).

We applied to the $\Psi(t)$ light curves a standard procedure[36] to solve the 180° ambiguity of Ψ. By assuming that temporal variations of Ψ are gradual, we minimized the variation $\Delta_n\Psi$ (where n indexes each individual time bins) between consecutive points Ψ_n and Ψ_{n+1} as follows. For two consecutive data points, $\Delta_n\Psi$ was defined as $|\Psi_{n+1}-\Psi_n|-\sqrt{\sigma^2(\Psi_{n+1})+\sigma^2(\Psi_n)^2}$, where $\sigma(\Psi_{n+1})$ and $\sigma(\Psi_n)$ are the errors for the consecutive angles considered. If $\Delta_n\Psi$ was larger than 90°, we shifted Ψ_{n+1} by multiples of ±180° as needed to minimize $\Delta_n\Psi$. Otherwise, when $\Delta_n \leq 90°$, we left Ψ_{n+1} unshifted. This procedure serves only for clarity of displaying the data, and is not critical for our estimation of the rotation rate, which was performed using unbinned event data or Stokes-parameter time series (see below).

γ-ray data. We studied the γ-ray activity of Mrk 421, analysing data collected with the Fermi-LAT in the energy range 0.1–100 GeV. We made use of the 3-day cadence light curve (within the years 2021 and 2022), which was extracted from the LAT Light Curve Repository, as shown in Fig. 3. We refer to ref. 67 for the detailed description of the unbinned maximum-likelihood data analysis. For this work, we adopted the light curve that was obtained using the option of leaving the spectral slope free to vary in the fit.

X-ray flux and continuum spectrum. We monitored the X-ray (0.3–10.0 keV) flux and spectral variations of Mrk 421 both near the time of and simultaneously with the IXPE pointings of May–June 2022 using the Neil Gehrels Swift-XRT (Supplementary Table 1). The Swift-XRT observations each had an exposure time of ~1 ks and were performed in windowed-timing mode. The data were processed using the XRT Data Analysis Software (v. 3.6.1). In the analysis, we used the latest calibration files available in the Swift-XRT CALibration DataBase (CALDB version 20210915). The X-ray source spectrum was extracted from the cleaned event file using a circular region with a radius of 47″. The background was extracted using a circular region with the same radius from a blank sky windowed-timing observation available in the Swift archive. As a final step, we binned the 0.3–10 keV data to achieve at least 25 counts in each energy bin.

For our spectral analysis, we used the Xspec program[68]. In all our fits, we included Galactic absorption along the line of sight ($N_H = 1.34\times10^{20}$ cm^{-2} (ref. 69)) using the TBABS model, with Fe abundances set according to ref. 70. For all the datasets, we found that a log-parabolic model, where the photon index varies as a log-parabola in energy (that is, $N(E) = K(E/E_p)^{(\alpha-\beta\log(E/E_p))}$ (ref. 71)), fits the spectra better than a simple power law (with $\Delta\chi^2$ in the range between −23 and −233, for one additional degree of freedom). In the log-parabolic model, the pivot energy E_p is a scaling factor, α is the spectral slope at the pivot energy, β corresponds to the spectral curvature and K is a normalization constant. In our fits, we set the pivot E_p to 5.0 keV (refs. 32,72), so that α approximates the photon index in the 3.0–7.0 keV range. In this way, we extracted the X-ray spectral evolution of Mrk 421 in May–June 2022 (Supplementary Fig. 1), including soft (S band, 0.3–2.0 keV) and hard (H band, 2.0–10.0 keV) X-ray fluxes, hardness ratio (H − S/H + S), and α and β parameters.

Within the IXPE pointing of May 2022, the X-ray flux rose by a factor of about two with no significant change in spectral shape[32]. Conversely, during the two IXPE pointings of June 2022, the flux increased from ~7.5×10^{-10} erg s^{-1} cm^{-2} at the beginning of Obs. 2 to the brightest point of ~1.4×10^{-9} erg s^{-1} cm^{-2} at the beginning of Obs. 3, and then decreased back to the previous level. The maximum variation of the soft flux was by a factor of ~1.2, while the hard flux varied by a factor of ~3. This is in agreement with the IXPE measurement in the 2.0–8.0 keV band, where the flux of Obs. 3 was about twice as high as during Obs. 2 (Table 1). Therefore, the spectrum became harder and flatter (that is, α decreased while the hardness ratio increased), with the flattest spectral shape coinciding with the brightest point.

Optical and infrared data. All the optical, infrared and radio/millimetre polarization measurements of Mrk 421 in the time frame of the IXPE pointings are shown in Fig. 1. Polarization observations in the optical were performed simultaneously with the IXPE pointings using the Hiroshima Optical and Near-InfraRed camera (HONIR) at the Kanata telescope, RoboPol at the Skinakas Observatory 1.3-m telescope[73], the Alhambra Faint Object Spectrograph and Camera (ALFOSC) mounted at the 2.5 m NOT, and the T90 telescope at the Sierra Nevada Observatory (SNO) during May–June 2022 in the R band (λ = 6,500 Å/E = 1.9 eV, full-width at half-maximum = 1,300 Å/0.4 eV). The HONIR observations were performed in three optical bands (http://hasc.hiroshima-u.ac.jp/instruments/honir/filters-e.html). The Stokes parameters are estimated by rotating the half-wave plate to four position angles and combining the exposures. The instrument and data analysis are described in detail in refs. 74,75. RoboPol is a novel four-channel opto-polarimeter with no moving parts and with the ability to measure the normalized Stokes q and u parameters with a single exposure simultaneously. A detailed description of the semi-automated analysis and data reduction pipeline can be found in refs. 38,76. The NOT data were reduced using the pipeline developed at the Tuorla Observatory, which follows standard photometric procedures[77,78]. We performed the SNO observations with polarized R_c filters, and calibrated the data using polarized and unpolarized standard stars. For the RoboPol, HONIR and NOT observations in the R band, we corrected for the host-galaxy depolarization by subtracting the (presumed unpolarized) host-galaxy flux density estimated for the individual apertures used in each observation[79]): $\Pi_{intr} = \Pi_{obs}\times I/(I - I_{host})$, where Π_{intr} and Π_{obs} are the intrinsic and observed polarization degree, respectively, I is the total flux density in mJy, and I_{host} is the host-galaxy flux density in mJy for the aperture of the observation[77].

The infrared observations were performed in the H band with the 1.8 m Boston University Perkins telescope (Flagstaff, AZ) using the infrared camera MIMIR in May–June 2022, supplemented by H-band HONIR observations in May 2022. The MIMIR instrument and data reduction procedures are described in detail in ref. 80. The Perkins H-band observations were corrected for the host-galaxy contribution following the prescription above. To find the contribution of the host galaxy for the aperture necessary for the correction, we performed a photometric decomposition of the galaxy light using the IMFIT package[81]. The model for the image decomposition consisted of a Sersic

profile for the host galaxy plus a point source for the blazar, determined by fitting a Moffat function[82] to several isolated stars in the image to create an average point-source function. We determined the parameters of the host galaxy as $n = 1.18 \pm 0.35$ for the Sersic index, an ellipticity of $e = 0.238 \pm 0.03$, an effective radius of $r_e = 2.1'' \pm 0.14''$, and a surface brightness of $\mu_e = 16.59 \pm 0.17$. For the average aperture diameter of 5.2″ used for the polarization observations, we estimated the contribution of the host-galaxy to be 12.41 ± 0.06 mag. Any additional infrared observations have not been corrected for the host-galaxy contribution, and hence should be considered as lower limits to the intrinsic polarization degree. All the optical/infrared observations are listed in Table 1.

Radio/millimetre data. Images of Mrk 421 at 7 mm wavelength with a resolution of ~0.2 mas, corresponding to 0.12 pc, were produced with data from VLBA observations at epochs 30 April, 5 June and 24 June 2022. The observations were from the Blazars Entering the Astrophysical Multi-Messenger Era (BEAM-ME) programme (see website www.bu.edu/blazars/BEAM-ME.html). The data acquisition and analysis are described in ref. 83. Supplementary Fig. 2 presents the images, in which total intensity is indicated by contours, polarized intensity by colour coding and polarization direction by yellow line segments. (Note that the 30 April image has lower dynamic range than the others, hence the jet is not as apparent.) The images reveal a change in the polarization direction of the 'core' (feature of peak intensity) between 30 April and the June epochs. The 5 June image exhibits some fanning out of the polarization vectors on the southeast side of the core, indicating an azimuthal component to the magnetic field, as one would expect if that component were helical. However, at the location of the 7 mm core, this component is weak relative to a more randomly oriented magnetic-field component.

Polarization at the shorter wavelengths of 3.5 mm (86.24 GHz) and 1.3 mm (230 GHz) was measured with the 30 m telescope of IRAM, located at the Pico Veleta Observatory (Sierra Nevada, Granada, Spain), on several nights in May–June 2022, as listed in Table 1. The observations were obtained within the Polarimetric Monitoring of AGN at Millimetre Wavelengths (POLAMI) programme[84,85] following the reduction and calibration pipeline described in detail in ref. 84.

No significant polarization at 1.3 mm from Mrk 421 was detected by IRAM either in May or June 2022, with an upper limit (at a confidence level of 95%) of <6% and <4%, respectively. The early May 3.5 mm observations are consistent within uncertainties with an average $\Pi_R = 3.4 \pm 0.7\%$ at an average $\psi_R = 54.5 \pm 6°$. The 30 May 2022 observation shows an increase in the polarization degree to $\Pi_R = 7.9 \pm 0.9$, with a polarization angle almost perpendicular to the early May observations ($\psi = 128 \pm 2.4°$). The subsequent observation shows a similar Π_R to the early May observations (1.76 ± 0.6%) at a roughly consistent angle of $\psi = 116 \pm 9°$. We obtained additional observations at 1.3 mm (225.538 GHz) using the SMA[86] within the SMA Monitoring of AGNs with Polarization (SMAPOL) programme. SMAPOL follows the polarization evolution of 40 γ-ray bright blazars, including Mrk 421, on a bi-weekly cadence, as well as other sources in a target-of-opportunity mode, including objects observed by IXPE. The Mrk 421 observations reported here were conducted on 4 June and 16 June 2022. The SMA observations employed two orthogonally polarized receivers, tuned to the same frequency range in full polarization mode, and used the SWARM correlator[87]. These receivers are inherently linearly polarized, but are converted to circular polarization by using the quarter-wave plates of the SMA polarimeter[88]. The lower sideband and upper sideband covered 209–221 GHz and 229–241 GHz, respectively. Each sideband was divided into six sub-bands with bandwidths of 2 GHz and a fixed channel width of 140 kHz. The SMA data were calibrated with the MIR software package (https://lweb.cfa.harvard.edu/~cqi/mircook.html). Instrumental polarization leakage was calibrated independently for the upper sideband and the lower sideband using the MIRIAD task gpcal[89] and removed from the data. The polarized intensity, position angle and percentage were derived from the Stokes I, Q and U visibilities. Between 4 and 16 June 2022, Mrk 421 decreased slightly in total flux, with values of 0.20 ± 0.02 Jy and 0.14 ± 0.02 Jy on 4 and 16 June, respectively. The linear polarization remained stable within the uncertainties between the two epochs, with a linear polarization degree of 2.3 ± 0.2% and 2.3 ± 0.3% and a polarization angle of 129.6 ± 2.6° and 132.6 ± 3.9° on 4 and 16 June, respectively. MWC 349 A was used for the total flux calibration, and the calibrator 3C 286, which has a high linear polarization degree and stable polarization angle, was observed in both sessions as a cross-check of the polarization calibration.

X-ray polarization analysis

Time-averaged IXPE data. The analysis of the first IXPE observation of Mrk 421, which discovered an X-ray polarization $\Pi_X = 15\% \pm 2\%$ at a polarization angle $\Psi_X = 35° \pm 4°$, is reported in ref. 32. Conversely, the X-ray polarization of Mrk 421 was undetected in the IXPE data of Obs. 2 and 3 when time-averaged over the entire length of the observations. Using the procedure of ref. 66 within ixpeobssim, we found for the 2.0–8.0 keV band data a nominal minimum detectable polarization (equivalent to a 99% confidence upper limit) of 5% and 4% for Obs. 2 and 3, respectively. Supplementary Fig. 3 shows the two-dimensional confidence contours for the X-ray polarization degree and angle obtained with the same method, to visually illustrate the lack of constraints on the X-ray polarization angle in these time-averaged data. A spectropolarimetric fit[90] of the data gives similar upper bounds for the polarization properties, assuming that the polarization degree and angle are constant with energy (using the polconst model in Xspec). A log-parabolic model best fits the I spectra, where we used the same fixed pivot energy as for the Swift-XRT data, $E_p = 5.0$ keV (see above). The IXPE data follow the same harder-when-brighter trend as for the Swift-XRT data: $\alpha = 3.17 \pm 0.06$, $\beta = 0.7 \pm 0.1$ and $\alpha = 2.81 \pm 0.03$, $\beta = 0.61 \pm 0.03$, for Obs. 2 and 3, respectively.

In the following, we investigate the cause of the change in the polarization properties of Mrk 421. The non-detection of the X-ray polarization of Mrk 421 in time-averaged IXPE Obs. 2 and 3 data can be due to time variability of the polarization angle within the observation (see, for example, ref. 25). A rotation of the polarization angle, as often observed for blazars in the optical band, can in principle cancel the polarization degree in time-averaged data. In the following, we test this hypothesis using a simple model where the polarization angle rotates at a constant rate while the polarization degree remains constant. This assumption is sufficient to our aim, which is to assess the reality of the polarization angle rotation. Consideration of more complex models for the time variability is beyond the scope of this paper. To make this assessment, we employ three methods: (1) a maximum-likelihood, unbinned event-based method, as in ref. 91; (2) a fit of the binned light curves of the Stokes parameters using χ^2 statistics; and (3) a fit of a rotation pattern in the Q–U plane using χ^2 statistics. A by-product of this analysis is an estimation of the rotation rate, for which all three methods return consistent results.

Searching for the optimal rotation rate via a likelihood analysis. For a detailed treatment of the optimal estimation of the (normalized) Stokes parameters q and u in the case of unbinned polarimetric data via a likelihood analysis, we refer the reader to ref. 91. An unbinned likelihood analysis is appropriate for fitting X-ray event data because of the Poisson nature of the counting statistics. This method has the advantage of being independent of any subjective choice of the binning of the data in energy or time.

Here we expand the likelihood analysis method to the case of a rotating polarization angle. The log-likelihood formula for the polarization parameters of a set of (Poisson distributed) events depends on the Stokes parameters as

$$S(q,u) = -2\sum_i \ln(1 + q\mu_i \cos 2\Psi_i + u\mu_i \sin 2\Psi_i), \quad (1)$$

where the sum is over each event i, μ_i is the modulation factor for event i (at energy E_i), Ψ_i is the event's instrumental phase angle, and it is assumed that q and u do not depend on the source flux. In addition, we are not fitting for the parameters of the spectral model.

As the time-averaged polarization is small and the apparent rotation is smooth, we can approximate the time behaviour with a simple model that has a varying polarization vector of constant degree, rotating at constant rate $\dot{\Psi}$. We also assume that there is no steady non-rotating component of the polarization (that is, $q_0 = u_0 = 0$). For this model, the likelihood can be written as

$$S(\dot{\Psi}, q, u) = -2\sum_i \ln\{1 + q\mu_i \cos[2\dot{\Psi}(t_i - t_0)] + u\mu_i \sin[2\dot{\Psi}(t_i - t_0)]\}, \quad (2)$$

where t_0 is a reference time, such as the midpoint of the observation period, and t_i is the time of event i. For any given rotation rate $\dot{\Psi}$, one can determine the optimal Stokes parameters $\hat{q}_r$ and $\hat{u}_r$ (where r indexes the the given rotation rate) by marginalizing over q and u and substituting $\hat{q}_r$ and $\hat{u}_r$ back into equation (2) to yield $S'(\dot{\Psi})$. The best-fit value of $\dot{\Psi}$, $\hat{\dot{\Psi}}$, is given by the minimum of $S'(\dot{\Psi})$ and, for Gaussian-distributed errors, uncertainties can be determined using $\Delta S'(\dot{\Psi}) = S'(\dot{\Psi}) - S'(\hat{\dot{\Psi}})$, since $\Delta S'(\dot{\Psi})$ is distributed as χ^2 with one degree of freedom, being a function of only one interesting parameter. Furthermore, we can compute the significance that $\hat{\dot{\Psi}}$ is non-zero using

$$\Delta S'(0) = S'(0) - S'(\hat{\dot{\Psi}}) = S(0, \hat{q}_0, \hat{u}_0) - S(\hat{\dot{\Psi}}; \hat{q}_r, \hat{u}_r). \quad (3)$$

Again, by marginalizing over q and u to test against the hypothesis that $\dot{\Psi} = 0$, $\Delta S'(0)$ is distributed as χ^2 with one degree of freedom.

We searched for the minima of $\Delta S(\dot{\Psi})$ over a grid of values of $\dot{\Psi}$, which we set to be −1,000° per day to +1,000° per day using the IXPE event files of the three observations of Mrk 421. Upon determining the best-fit value of $\dot{\Psi}$, we estimated the uncertainty of the best-fit parameters at a confidence level of 90% using $\Delta S'(\dot{\Psi})$. The results of this analysis are show in Supplementary Fig. 4. As expected, for Obs. 1, the estimated rotation rate is consistent with null rotation ($\dot{\Psi} = -6 \pm 9°$ per day), while the estimated polarization degree ($\Pi_X = 15 \pm 2\%$) is consistent with our previous work[32]. Conversely, for Obs. 2 and 3 we find absolute minima of $\Delta S'(\dot{\Psi})$ at $\dot{\Psi} = 80 \pm 9°$ per day and $\dot{\Psi} = 91 \pm 8°$ per day, respectively, and that $\dot{\Psi} = 0$ is ruled out at better than 7σ for both observations. The estimated polarization degrees for these two datasets were both $\Pi_X = 10 \pm 1\%$, which suggests that while the polarization angle was rotating, the polarization degree may have remained similar to that measured when not rotating. The estimated rotation rates for Obs. 2 and 3 are consistent within the uncertainties, which suggests that we may have sampled two segments of one continuous rotation event spanning three days. Combining Obs. 2 and 3, we found a rotation rate of $R = 77.0 \pm 2.4°$ per day and $\Pi_X = 10.1 \pm 0.8\%$, indicating that the third observation was approximately in phase with the second after a day passed.

Modelling the time-binned Stokes parameters. As a second test of the hypothesis of polarization angle rotation cancelling the polarization degree in the time-averaged data, we modelled the time series of the normalized Stokes parameters. As in ref. 32, to investigate the polarization variability on different timescales, we used the temporal variations of the normalized Stokes parameters $q(t)$ and $u(t)$ with various time bin sizes in the range from ~8 ks (corresponding to $N_{bins} = 20$ bins) to ~60 ks ($N_{bins} = 3$). We fit all the time series with (1) a constant model and (2) a model where the polarization angle rotates at a constant rate $\dot{\Psi}$ while the polarization degree Π remains constant, such that the Stokes parameters vary as trigonometric functions: $q(t) = \Pi \cos(2(\dot{\Psi}t + \phi))$ and $u(t) = \Pi \sin(2(\dot{\Psi}t + \phi))$ (where ϕ is a phase angle). As a test of the goodness of the fits, we computed, for all the cases tested, the probability for the null hypothesis (P_{null}) to obtain by chance a χ^2 value at least as large as that measured if the data are drawn according to the model.

Supplementary Fig. 5 shows, for both IXPE observations and for all the tested time binning schemes, the P_{null} values obtained for the constant model (black symbols) and the constant rotation model (red symbols). A constant model is statistically unacceptable ($P_{null} < 1\%$) for any time binning. A model including a linear time variation of the polarization angle always provides a better fit (that is, an increase of P_{null}, up to ~99% in several cases) than a constant model. Supplementary Fig. 6 shows all the fit realizations, for the case N_{bins} in the range between 3 and 20. In our fitting exercise, we keep the parameters $\dot{\Psi}$ and Π fixed to those determined from the likelihood analysis. Hence, ϕ is the only free parameter. Moreover, we note that the independent fits of $q(t)$ and $u(t)$ return best-fit values of ϕ consistent within each other (within a typical uncertainty of ~8°). This is an a posteriori indication that our fits are physical. To further assess the phenomenology of the polarization variability, we allow, in turn, the rotation rate $\dot{\Psi}$ and the polarization degree Π to be free in our fits. We find that $\dot{\Psi}$ is unconstrained in these fits. Conversely, the best fit corresponds to values of Π that are marginally inconsistent between the fit of $q(t)$ (for example, $\Pi = 11\% \pm 2\%$ for the case $N_{bins} = 16$) and that of $u(t)$ (for example, $\Pi = 5\% \pm 2\%$). This suggests that Π and/or $\dot{\Psi}$ are somewhat variable with time about the average values, rather than constant. The detailed modelling of these variability features is beyond the scope of our hypothesis testing, and may be assessed in future works in the context of physically motivated models.

Fitting a rotation model in the Q–U plane

As a third and final test, we modelled the time behaviour of the data in the Q–U plane, with $N_{bins} = 24$. We display the time evolution of the data in Supplementary Fig. 7. In this framework, as a first, straightforward test for variability, we calculated the χ^2 statistic for the mean Q/U Stokes parameters in each time bin under the null hypothesis that they are all consistent with the time-integrated mean Stokes parameters ($\bar{Q}$ and $\bar{U}$). As the Stokes parameters from each time bin (denoted as Q_i and U_i, respectively, for time bin i) are normally distributed and independent, the quantity

$$\chi^2 = \sum_i \frac{(Q_i - \bar{Q})^2 + (U_i - \bar{U})^2}{\sigma_i^2} \quad (4)$$

under this null hypothesis follows a χ^2 distribution with $2N_{bins} - 2 = 46$ degrees of freedom. We can therefore compare the observed value of χ^2 with the expected values. For Obs. 1, we find $\chi^2 = 55$, the probability of which arising from the null hypothesis of constant Stokes parameters is $P_{null} \approx 0.17$, suggesting that these data are consistent with the constant polarization model. Conversely, for Obs. 2 and 3, we determine χ^2 values of 78 and 121, respectively. The probability of acquiring χ^2 exceeding this value by chance under the null hypothesis of constant polarization is $P_{null} < 2 \times 10^{-3}$. This implies that, in these cases, the null hypothesis can be rejected with high confidence.

Using this same statistical framework, we are able to determine the best-fit rotation rate $\dot{\Psi}_X$ for the model by assuming that both $\dot{\Psi}_X$ and the polarization degree are constant (see above for the mathematical form of this model). When applying these calculations to the data of Obs. 1, we find no evidence of time-dependent rotation of Ψ_X: the best-fit constant rotation rate is −4 ± 7° per day). For Obs. 2 and 3, the best-fit rotation rates are $\dot{\Psi}_X = 78 \pm 8°$ per day and $83 \pm 6°$ per day, respectively. These values are consistent with the findings of the previously described methods using the same model, indicating that all three methods result in a consistent rate of rotation. The corresponding χ^2 value for each of these fits is 53 for 45 degrees of freedom, with a corresponding value of $P_{null} \approx 0.18$. We can therefore conclude that a constant rotation model provides a good fit to the data. Attempts to fit these data to a more complex elliptical rotation model (that is, where the polarization degree varies with time) do not result in a statistically

significant improvement in the overall value of χ^2 given the reduced degrees of freedom.

Comparison with a stochastic model

To verify further our explanation of the cause of the X-ray polarization angle rotation in Mrk 421, we tested the hypothesis that the rotation occurred by chance as a result of a stochastic variation of Ψ_X. We considered two possibilities for the involvement of random processes. First, the variations in Ψ_X during the two IXPE observations of June corresponded to two independent rotations. Second, the two IXPE observations were part of one continuous rotation, of which we sampled only two segments. To determine the probability of the rotation(s) occurring by chance due to the random variations of Ψ_X, we simulated the time dependence of the polarization degree and angle that occur via random walks, and compared them with the IXPE results. As described in detail in refs. 52,53, the simulations are based on two parameters: the number of maximally polarized (that is, each with uniform magnetic field) cells, N_{cell}, and the number of cells that change per day, N_{Var}. The cells each have the same intensity, hence the total intensity $I_{total} = N_{cell}I$. The initial Stokes parameters Q and U for each cell were drawn from Gaussian distributions. At every simulation time step, one cell was selected randomly, and its Q and U values were drawn anew, then the averages of Q, U, Π and Ψ over all cells were calculated anew. The number of simulated time steps depends on the observation duration and (N_{Var}); for example, for $N_{Var} = 100$ we simulated 100 data points per day. For each of the aforementioned possibilities, we performed a grid search in the N_{cell}, N_{Var} parameter space to identify episodes of rotation of Ψ.

For the first case, we set the total length of the simulated polarization light curves to the length of each of the IXPE observations. We created 10,000 simulated light curves, binned to match one of the data binning schemes, and recorded the average Π of the light curve and the longest continuous variation of Ψ that could be interpreted as a rotation. We considered a trial successful if the average Π and standard deviation of the simulated time dependence was within 10% of the observed values, and if the variation in Ψ was equal to or larger than that observed. Supplementary Figs. 8 and 9 show the results for the parameter search of each event. The binning of the data can have a significant effect on the number of successful trials. For that reason, we repeated the analysis for different numbers of bins from 3 to 18. For IXPE Obs. 2 (first rotation) we found that the P significance values to range from 0.0049 to 0.14 (13 bins), with a median of 0.057. For the following rotation (IXPE Obs. 3), we found $P = 0.0013$ to 0.21 (17 bins), with a median of 0.032. The probability of two independent events occurring by pure chance in a row is then $P = 0.029$.

For the second possibility, we set the length of the simulated light curves equal to the total duration of the observations from the beginning of IXPE Obs. 2 to the end of Obs. 3. To test the case of an individual rotation, the polarization angle curve of Obs. 3 was shifted by ±180° as needed to align the two segments. In this case, we explored from 3 to 26 bins and additionally required that the rotation rate of the second segment lie within 10% of that of the first segment. We repeated the above procedure and estimated the number of successful trials (Supplementary Fig. 10). We find $P = 0.0006$ to 0.022 (23 bins) with a median of 0.0053. All of the above results indicate that it is unlikely that the observed rotation(s) were caused by a purely stochastic process. Rather, the event has a high probability of being related to non-stochastic physical processes in the jet.

Activity state of Mrk 421

In Supplementary Fig. 11, we show the long-term light curves of Mrk 421 in optical brightness (top panel) from the Steward Observatory monitoring programme[92] and ATLAS[93–95], as well as the X-ray flux (bottom panel) from the Swift-XRT. The optical observations cover a time range from 2006 to 2022 and we highlight as vertical grey lines the time of the IXPE pointings.

The Swift-XRT observations are in the 0.3–10 keV band. The minimum and maximum value of the X-ray flux were 0.5×10^{-10} erg s^{-1} cm^{-2} and 55×10^{-10} erg s^{-1} cm^{-2}, respectively, with a median value of 8.5×10^{-10} erg s^{-1} cm^{-2}. As a comparison, the flux measured by Swift at the time of the IXPE pointings (Supplementary Table 1) ranged between 7.5×10^{-10} and 14.1×10^{-10} erg s^{-1} cm^{-2}. Thus, we conclude that Mrk 421 was at an average level of X-ray activity at the time of the IXPE observations.

We show the optical brightness in the top panel of Supplementary Fig. 11. The Steward Observatory observations are in the R band, while for ATLAS we show both c-band and o-band observations. While the Steward and ATLAS observations are not directly comparable without applying conversion factors between optical bands, it is evident from the overlap of the two surveys (2016–2018) that any difference is rather small compared with the overall brightness variations of Mrk 421. The ATLAS observations in 2022 are ~0.5 mag lower than the average of the Steward observations (2011–2016) and ~1-5 mag lower than the flares seen in the Steward data. Therefore, we can also conclude that the optical brightness of Mrk 421 at the time of the IXPE observations was at an average state.

Data availability

The data that support the findings of this study are either publicly available at the HEASARC database or available from the corresponding author upon request.

Code availability

The ixpeobssim software and documentation can be downloaded at https://github.com/lucabaldini/ixpeobssim.

References

1. Blandford, R., Meier, D. & Readhead, A. Relativistic jets from active galactic nuclei. *Annu. Rev. Astron. Astrophys.* **57**, 467–509 (2019).
2. Romero, G. E., Boettcher, M., Markoff, S. & Tavecchio, F. Relativistic jets in active galactic nuclei and microquasars. *Space Sci. Rev.* **207**, 5–61 (2017).
3. Blandford, R. & Eichler, D. Particle acceleration at astrophysical shocks: a theory of cosmic ray origin. *Phys. Rep.* **154**, 1–75 (1987).
4. Sironi, L. & Spitkovsky, A. Relativistic reconnection: an efficient source of non-thermal particles. *Astrophys. J. Lett.* **783**, L21 (2014).
5. Bodo, G., Tavecchio, F. & Sironi, L. Kink-driven magnetic reconnection in relativistic jets: consequences for X-ray polarimetry of BL Lacs. *Mon. Not. R. Astron. Soc.* **501**, 2836–2847 (2021).
6. Zhang, H. et al. Radiation and polarization signatures from magnetic reconnection in relativistic jets. I. A systematic study. *Astrophys. J.* **901**, 149 (2020).
7. Comisso, L. & Sironi, L. Particle acceleration in relativistic plasma turbulence. *Phys. Rev. Lett.* **121**, 255101 (2018).
8. Angel, J. R. P. & Stockman, H. S. Optical and infrared polarization of active extragalactic objects. *Annu. Rev. Astron. Astrophys.* **18**, 321–361 (1980).
9. Blinov, D. et al. RoboPol: first season rotations of optical polarization plane in blazars. *Mon. Not. R. Astron. Soc.* **453**, 1669–1683 (2015).
10. Blinov, D. et al. RoboPol: connection between optical polarization plane rotations and gamma-ray flares in blazars. *Mon. Not. R. Astron. Soc.* **474**, 1296–1306 (2018).
11. Larionov, V. M. et al. The outburst of the blazar S5 0716+71 in 2011 October: shock in a helical jet. *Astrophys. J.* **768**, 40 (2013).
12. Vlahakis, N. Disk–jet connection. In *Blazar Variability Workshop II: Entering the GLAST Era*, *Astronomical Society of the Pacific Conference Series* Vol. 350 (eds Miller, H. R. et al.) 169–177 (Astronomical Society of the Pacific, 2006).
13. Marscher, A. P. et al. The inner jet of an active galactic nucleus as revealed by a radio-to-γ-ray outburst. *Nature* **452**, 966–969 (2008).

14. Marscher, A. P. et al. Probing the inner jet of the quasar PKS 1510−089 with multi-waveband monitoring during strong gamma-ray activity. *Astrophys. J. Lett.* **710**, L126–L131 (2010).
15. Zhang, S. et al. Hard X-ray morphological and spectral studies of the galactic center molecular cloud Sgr B2: constraining past Sgr A* flaring activity. *Astrophys. J.* **815**, 132 (2015).
16. Zhang, H., Deng, W., Li, H. & Böttcher, M. Polarization signatures of relativistic magnetohydrodynamic shocks in the blazar emission region. I. Force-free helical magnetic fields. *Astrophys. J.* **817**, 63 (2016).
17. Hovatta, T. et al. MOJAVE: Monitoring of Jets in Active Galactic Nuclei with VLBA Experiments. VIII. Faraday rotation in parsec-scale AGN jets. *Astron. J.* **144**, 105 (2012).
18. Gabuzda, D. C. Inherent and local magnetic field structures in jets from active galactic nuclei. *Galaxies* **9**, 58 (2021).
19. Liodakis, I. et al. Two flares with one shock: the interesting case of 3C 454.3. *Astrophys. J.* **902**, 61 (2020).
20. D'Arcangelo, F. D. et al. Rapid multiwaveband polarization variability in the quasar PKS 0420-014: optical emission from the compact radio jet. *Astrophys. J. Lett.* **659**, L107–L110 (2007).
21. Peirson, A. L. & Romani, R. W. The polarization behavior of relativistic synchrotron jets. *Astrophys. J.* **864**, 140 (2018).
22. Marscher, A. P. Turbulent, extreme multi-zone model for simulating flux and polarization variability in blazars. *Astrophys. J.* **780**, 87 (2014).
23. Marscher, A. P. in *Extragalactic Jets from Every Angle* Vol. 313 (eds Massaro, F. et al.) 122–127 (Cambridge Univ. Press, 2015).
24. Marscher, A. P. & Jorstad, S. G. Frequency and time dependence of linear polarization in turbulent jets of blazars. *Galaxies* **9**, 27 (2021).
25. Di Gesu, L. et al. Testing particle acceleration models for BL Lac jets with the Imaging X-ray Polarimetry Explorer. *Astron. Astrophys.* **662**, A83 (2022).
26. Abdo, A. A. et al. Fermi Large Area Telescope observations of Markarian 421: the missing piece of its spectral energy distribution. *Astrophys. J.* **736**, 131 (2011).
27. Lin, Y. C. et al. Detection of high-energy gamma-ray emission from the BL Lacertae object Markarian 421 by the EGRET Telescope on the Compton Observatory. *Astrophys. J. Lett.* **401**, L61 (1992).
28. Punch, M. et al. Detection of TeV photons from the active galaxy Markarian 421. *Nature* **358**, 477–478 (1992).
29. Giommi, P. et al. X-ray spectra, light curves and SEDs of blazars frequently observed by Swift. *Mon. Not. R. Astron. Soc.* **507**, 5690–5702 (2021).
30. Middei, R. et al. The first hard X-ray spectral catalogue of blazars observed by NuSTAR. *Mon. Not. R. Astron. Soc.* **514**, 3179–3190 (2022).
31. Donnarumma, I. et al. The June 2008 flare of Markarian 421 from optical to TeV energies. *Astrophys. J. Lett.* **691**, L13–L19 (2009).
32. Di Gesu, L. et al. The X-ray polarization view of Mrk~421 in an average flux state as observed by the Imaging X-ray Polarimetry Explorer. *Astrophys. J. Lett*. https://doi.org/10.3847/2041-8213/ac913a (2022).
33. Liodakis, I. et al. Polarized blazar X-rays imply particle acceleration in shocks. *Nature* https://doi.org/10.1038/s41586-022-05338-0 (2022).
34. Marscher, A. P. et al. The inner jet of an active galactic nucleus as revealed by a radio-to-γ-ray outburst. *Nature* **452**, 966–969 (2008).
35. Marscher, A. P. et al. Probing the inner jet of the quasar PKS 1510−089 with multi-waveband monitoring during strong gamma-ray activity. *Astrophys. J. Lett.* **710**, L126–L131 (2010).
36. Blinov, D. et al. RoboPol: first season rotations of optical polarization plane in blazars. *Mon. Not. R. Astron. Soc.* **453**, 1669–1683 (2015).
37. Blinov, D. et al. RoboPol: connection between optical polarization plane rotations and gamma-ray flares in blazars. *Mon. Not. R. Astron. Soc.* **474**, 1296–1306 (2018).
38. Blinov, D. et al. RoboPol: AGN polarimetric monitoring data. *Mon. Not. R. Astron. Soc.* **501**, 3715–3726 (2021).
39. Atwood, W. B. et al. The Large Area Telescope on the Fermi Gamma-Ray Space Telescope Mission. *Astrophys. J.* **697**, 1071–1102 (2009).
40. Tavecchio, F. Probing magnetic fields and acceleration mechanisms in blazar jets with X-ray polarimetry. *Galaxies* **9**, 37 (2021).
41. Kiehlmann, S. et al. The time-dependent distribution of optical polarization angle changes in blazars. *Mon. Not. R. Astron. Soc.* **507**, 225–243 (2021).
42. MAGIC Collaboration et al. Multi-wavelength characterization of the blazar S5 0716+714 during an unprecedented outburst phase. *Astron. Astrophys.* **619**, A45 (2018).
43. Hughes, P. A., Aller, H. D. & Aller, M. F. Polarized radio outbursts in BL Lacertae. II. The flux and polarization of a piston-driven shock. *Astrophys. J.* **298**, 301–315 (1985).
44. Tavecchio, F., Landoni, M., Sironi, L. & Coppi, P. Probing shock acceleration in BL Lac jets through X-ray polarimetry: the time-dependent view. *Mon. Not. R. Astron. Soc.* **498**, 599–608 (2020).
45. Kirk, J. G., Rieger, F. M. & Mastichiadis, A. Particle acceleration and synchrotron emission in blazar jets. *Astron. Astrophys.* **333**, 452–458 (1998).
46. Georganopoulos, M. & Kazanas, D. Decelerating flows in TeV blazars: a resolution to the BL Lacertae-FR I unification problem. *Astrophys. J. Lett.* **594**, L27–L30 (2003).
47. Ghisellini, G., Tavecchio, F. & Chiaberge, M. Structured jets in TeV BL Lac objects and radiogalaxies. Implications for the observed properties. *Astron. Astrophys.* **432**, 401–410 (2005).
48. Chhotray, A. et al. On radiative acceleration in spine-sheath structured blazar jets. *Mon. Not. R. Astron. Soc.* **466**, 3544–3557 (2017).
49. Giroletti, M., Giovannini, G., Taylor, G. B. & Falomo, R. A sample of low-redshift BL Lacertae objects. II. EVN and MERLIN data and multiwavelength analysis. *Astrophys. J.* **646**, 801–814 (2006).
50. Piner, B. G., Pant, N. & Edwards, P. G. The jets of TeV blazars at higher resolution: 43 GHz and polarimetric VLBA observations from 2005 to 2009. *Astrophys. J.* **723**, 1150–1167 (2010).
51. Marscher, A. P. & Jorstad, S. G. Linear polarization signatures of particle acceleration in high-synchrotron-peak blazars. *Universe* **8**, 644 (2022).
52. Kiehlmann, S., Blinov, D., Pearson, T. J. & Liodakis, I. Optical EVPA rotations in blazars: testing a stochastic variability model with RoboPol data. *Mon. Not. R. Astron. Soc.* **472**, 3589–3604 (2017).
53. Kiehlmann, S. et al. Polarization angle swings in blazars: the case of 3C 279. *Astron. Astrophys.* **590**, A10 (2016).
54. Bodo, G., Tavecchio, F. & Sironi, L. Kink-driven magnetic reconnection in relativistic jets: consequences for X-ray polarimetry of BL Lacs. *Mon. Not. R. Astron. Soc.* **501**, 2836–2847 (2021).
55. Zhang, H., Li, X., Giannios, D. & Guo, F. First-principles prediction of X-ray polarization from magnetic reconnection in high-frequency BL Lacertae objects. *Astrophys. J.* **912**, 129 (2021).
56. Zhang, H. et al. Radiation and polarization signatures from magnetic reconnection in relativistic jets. II. Connection with γ-rays. *Astrophys. J.* **924**, 90 (2022).
57. Dong, L., Zhang, H. & Giannios, D. Kink instabilities in relativistic jets can drive quasi-periodic radiation signatures. *Mon. Not. R. Astron. Soc.* **494**, 1817–1825 (2020).
58. Jorstad, S. G. et al. Rapid quasi-periodic oscillations in the relativistic jet of BL Lacertae. *Nature* **609**, 265–268 (2022).

59. Peirson, A. L. & Romani, R. W. The polarization behavior of relativistic synchrotron jets. *Astrophys. J.* **864**, 140 (2018).
60. Angelakis, E. et al. RoboPol: the optical polarization of gamma-ray-loud and gamma-ray-quiet blazars. *Mon. Not. R. Astron. Soc.* **463**, 3365–3380 (2016).
61. Blinov, D. et al. RoboPol: do optical polarization rotations occur in all blazars? *Mon. Not. R. Astron. Soc.* **462**, 1775–1785 (2016).
62. Rankin, J. et al. An algorithm to calibrate and correct the response to unpolarized radiation of the X-ray polarimeter onboard IXPE. *Astron. J.* **163**, 39 (2022).
63. Ferrazzoli, R. et al. In-flight calibration system of imaging X-ray polarimetry explorer. *J. Astron. Telesc. Instrum. Syst.* **6**, 048002 (2020).
64. Pesce-Rollins, M., Lalla, N. D., Omodei, N. & Baldini, L. An observation–simulation and analysis framework for the Imaging X-ray Polarimetry Explorer (IXPE). *Nucl. Instrum. Methods Phys. Res. A* **936**, 224–226 (2019).
65. Baldini, L. et al. ixpeobssim: a simulation and analysis framework for the Imaging X-ray Polarimetry Explorer. *SoftwareX* https://doi.org/10.1016/j.softx.2022.101194 (2022).
66. Kislat, F., Clark, B., Beilicke, M. & Krawczynski, H. Analyzing the data from X-ray polarimeters with Stokes parameters. *Astropart. Phys.* **68**, 45–51 (2015).
67. Soheila, A. et al. The Fermi-LAT Light Curve Repository. *Astrophys. J.* https://doi.org/10.3847/1538-4365/acbb6a (2023).
68. Arnaud, K., Dorman, B. & Gordon, C. XSPEC: an X-ray spectral fitting package. *Astrophysics Source Code Library* ascl:9910.005 (1999).
69. HI4PI Collaboration et al. HI4PI: A full-sky H I survey based on EBHIS and GASS. *Astron. Astrophys.* **594**, A116 (2016).
70. Wilms, J., Allen, A. & McCray, R. On the absorption of X-rays in the interstellar medium. *Astrophys. J.* **542**, 914–924 (2000).
71. Massaro, E., Perri, M., Giommi, P. & Nesci, R. Log-parabolic spectra and particle acceleration in the BL Lac object Mkn 421: spectral analysis of the complete BeppoSAX wide band X-ray data set. *Astron. Astrophys.* **413**, 489–503 (2004).
72. Baloković, M. et al. Multiwavelength study of quiescent states of Mrk 421 with unprecedented hard X-ray coverage provided by NuSTAR in 2013. *Astrophys. J.* **819**, 156 (2016).
73. Ramaprakash, A. N. et al. RoboPol: a four-channel optical imaging polarimeter. *Mon. Not. R. Astron. Soc.* **485**, 2355–2366 (2019).
74. Kawabata, K. S. et al. A new spectropolarimeter at the Dodaira Observatory. *Publ. Astron. Soc. Pac.* **111**, 898–908 (1999).
75. Akitaya, H. et al. HONIR: an optical and near-infrared simultaneous imager, spectrograph, and polarimeter for the 1.5-m Kanata telescope. In *Ground-based and Airborne Instrumentation for Astronomy V*, *Society of Photo-Optical Instrumentation Engineers Conference Series* Vol. 9147 (eds Ramsay, S. K. et al.) 91474O (SPIE, 2014).
76. Panopoulou, G. et al. Optical polarization map of the Polaris Flare with RoboPol. *Mon. Not. R. Astron. Soc.* **452**, 715–726 (2015).
77. Hovatta, T. et al. Optical polarization of high-energy BL Lacertae objects. *Astron. Astrophys.* **596**, A78 (2016).
78. Nilsson, K. et al. Long-term optical monitoring of TeV emitting blazars. I. Data analysis. *Astron. Astrophys.* **620**, A185 (2018).
79. Nilsson, K. et al. Host galaxy subtraction of TeV candidate BL Lacertae objects. *Astron. Astrophys.* **475**, 199–207 (2007).
80. Clemens, D. P., Pinnick, A. F. & Pavel, M. D. Polarimetric calibration of Mimir and the Galactic Plane Infrared Polarization Survey (GPIPS). *Astrophys. J. Suppl. Ser.* **200**, 20 (2012).
81. Erwin, P. IMFIT: a fast, flexible new program for astronomical image fitting. *Astrophys. J.* **799**, 226 (2015).
82. Moffat, A. F. J. A theoretical investigation of focal stellar images in the photographic emulsion and application to photographic photometry. *Astron. Astrophys.* **3**, 455 (1969).
83. Jorstad, S. G. et al. Kinematics of parsec-scale jets of gamma-ray blazars at 43 GHz within the VLBA-BU-BLAZAR program. *Astrophys. J.* **846**, 98 (2017).
84. Agudo, I. et al. POLAMI: Polarimetric Monitoring of AGN at Millimetre Wavelengths—I. The programme, calibration and calibrator data products. *Mon. Not. R. Astron. Soc.* **474**, 1427–1435 (2018).
85. Agudo, I. et al. POLAMI: Polarimetric Monitoring of Active Galactic Nuclei at Millimetre Wavelengths—III. Characterization of total flux density and polarization variability of relativistic jets. *Mon. Not. R. Astron. Soc.* **473**, 1850–1867 (2018).
86. Ho, P. T. P., Moran, J. M. & Lo, K. Y. The Submillimeter Array. *Astrophys. J. Lett.* **616**, L1–L6 (2004).
87. Primiani, R. A. et al. SWARM: \ 32 GHz correlator and VLBI beamformer for the Submillimeter Array. *J. Astron. Instrum.* **5**, 1641006–810 (2016).
88. Marrone, D. P. & Rao, R. The submillimeter array polarimeter. In *Millimeter and Submillimeter Detectors and Instrumentation for Astronomy IV*, *Society of Photo-Optical Instrumentation Engineers Conference Series* Vol. 7020 (eds Duncan, W. D. et al.) J.70202B (SPIE, 2008).
89. Sault, R. J., Teuben, P. J. & Wright, M. C. H. a retrospective view of MIRIAD. *In Astronomical Data Analysis Software and Systems IV*, *Astronomical Society of the Pacific Conference Series* Vol. 77 (eds Shaw, R. A. et al.) 433 (1995).
90. Strohmayer, T. E. X-ray spectro-polarimetry with photoelectric polarimeters. *Astrophys. J.* **838**, 72 (2017).
91. Marshall, H. L. Analysis of polarimetry data with angular uncertainties. *Astron. J.* **162**, 134 (2021).
92. Smith, P. S. et al. Coordinated Fermi/optical monitoring of blazars and the great 2009 September gamma-ray flare of 3C 454.3. Preprint at *arXiv* https://doi.org/10.48550/arXiv.0912.3621 (2009).
93. Tonry, J. L. et al. ATLAS: a high-cadence all-sky survey system. *Publ. Astron. Soc. Pac.* **130**, 064505 (2018).
94. Heinze, A. N. et al. A first catalog of variable stars measured by the Asteroid Terrestrial-impact Last Alert System (ATLAS). *Astron. J.* **156**, 241 (2018).
95. Shingles, L. et al. Release of the ATLAS Forced Photometry server for public use. *Transient Name Server AstroNote* **7**, 1–7 (2021).

Acknowledgements

The Imaging X-ray Polarimetry Explorer (IXPE) is a joint US and Italian mission. The US contribution is supported by the National Aeronautics and Space Administration (NASA) and led and managed by its Marshall Space Flight Center (MSFC), with industry partner Ball Aerospace (contract NNM15AA18C). The Italian contribution is supported by the Italian Space Agency (Agenzia Spaziale Italiana, ASI) through contract ASI-OHBI-2017-12-I.0, agreements ASI-INAF-2017-12-H0 and ASI-INFN-2017.13-H0, and its Space Science Data Center (SSDC), and by the Istituto Nazionale di Astrofisica (INAF) and the Istituto Nazionale di Fisica Nucleare (INFN) in Italy. This research used data products provided by the IXPE Team (MSFC, SSDC, INAF and INFN) and distributed with additional software tools by the High-Energy Astrophysics Science Archive Research Center (HEASARC), at NASA Goddard Space Flight Center (GSFC). The IAA-CSIC group acknowledges financial support from the grant CEX2021-001131-S funded by MCIN/AEI/10.13039/501100011033 to the Instituto de Astrofísica de Andalucía-CSIC and through grant PID2019-107847RB-C44. The POLAMI observations were carried out at the IRAM 30 m Telescope. IRAM is supported by INSU/CNRS (France), MPG (Germany) and IGN (Spain). The Submillimetre Array is a joint project between the Smithsonian Astrophysical Observatory and the Academia Sinica Institute of Astronomy and Astrophysics and is funded by the Smithsonian Institution and the Academia Sinica. Mauna Kea, the location of the SMA, is a culturally important site

for the indigenous Hawaiian people; we are privileged to study the cosmos from its summit. Some of the data reported here are based on observations made with the Nordic Optical Telescope, owned in collaboration with the University of Turku and Aarhus University, and operated jointly by Aarhus University, the University of Turku and the University of Oslo, representing Denmark, Finland and Norway, the University of Iceland and Stockholm University at the Observatorio del Roque de los Muchachos, La Palma, Spain, of the Instituto de Astrofisica de Canarias. E.L. was supported by Academy of Finland projects 317636 and 320045. The data presented here were obtained (in part) with ALFOSC, which is provided by the Instituto de Astrofisica de Andalucia (IAA) under a joint agreement with the University of Copenhagen and NOT. We are grateful to V. Braga, M. Monelli and M. Sänchez Benavente for performing the observations at the Nordic Optical Telescope. Part of the French contributions is supported by the Scientific Research National Center (CNRS) and the French spatial agency (CNES). The research at Boston University was supported in part by National Science Foundation grant AST-2108622, NASA Fermi Guest Investigator grants 80NSSC21K1917 and 80NSSC22K1571, and NASA Swift Guest Investigator grant 80NSSC22K0537. This research was conducted in part using the Mimir instrument, jointly developed at Boston University and Lowell Observatory and supported by NASA, NSF and the W.M. Keck Foundation. We thank D. Clemens for guidance in the analysis of the Mimir data. This work was supported by JST, the establishment of university fellowships towards the creation of science and technology innovation, grant number JPMJFS2129. This work was supported by Japan Society for the Promotion of Science (JSPS) KAKENHI grant number JP21H01137. This work was also partially supported by the Optical and Near-Infrared Astronomy Inter-University Cooperation Program from the Ministry of Education, Culture, Sports, Science and Technology (MEXT) of Japan. We are grateful to the observation and operating members of the Kanata Telescope. Some of the data are based on observations collected at the Observatorio de Sierra Nevada, owned and operated by the Instituto de Astrofísica de Andalucía (IAA-CSIC). Further data are based on observations collected at the Centro Astronómico Hispano en Andalucía (CAHA), operated jointly by Junta de Andalucía and Consejo Superior de Investigaciones Científicas (IAA-CSIC). This research has made use of data from the RoboPol programme, a collaboration between Caltech, the University of Crete, IA-FORTH, IUCAA, the MPIfR and the Nicolaus Copernicus University, which was conducted at Skinakas Observatory in Crete, Greece. D.B., S.K., R.S. and N.M., acknowledge support from the European Research Council (ERC) under the European Unions Horizon 2020 Research and Innovation programme under grant agreement no. 771282. C.C. acknowledges support from the European Research Council (ERC) under the HORIZON ERC Grants 2021 programme under grant agreement no. 101040021. The research at Boston University was supported in part by National Science Foundation grant AST-2108622, NASA Fermi Guest Investigator grant 80NSSC21K1917 and 80NSSC22K1571, and NASA Swift Guest Investigator grant 80NSSC22K0537. This work was supported by NSF grant AST-2109127. We acknowledge the use of public data from the Swift data archive. Data from the Steward Observatory spectropolarimetric monitoring project were used. This programme is supported by Fermi Guest Investigator grants NNX08AW56G, NNX09AU10G, NNX12AO93G and NNX15AU81G. We acknowledge funding to support our NOT observations from the Finnish Centre for Astronomy with ESO (FINCA), University of Turku, Finland (Academy of Finland grant no 306531). This work has made use of data from the Asteroid Terrestrial-impact Last Alert System (ATLAS) project. The Asteroid Terrestrial-impact Last Alert System (ATLAS) project is primarily funded to search for near-Earth asteroids through NASA grants NN12AR55G, 80NSSC18K0284 and 80NSSC18K1575; by-products of the NEO search include images and catalogues from the survey area. This work was partially funded by Kepler/K2 grant J1944/80NSSC19K0112 and HST GO-15889, and STFC grants ST/T000198/1 and ST/S006109/1. The ATLAS science products have been made possible through the contributions of the University of Hawaii Institute for Astronomy, the Queen's University Belfast, the Space Telescope Science Institute, the South African Astronomical Observatory and The Millennium Institute of Astrophysics (MAS), Chile. The Very Long Baseline Array is an instrument of the National Radio Astronomy Observatory. The National Radio Astronomy Observatory is a facility of the National Science Foundation operated under a cooperative agreement by Associated Universities, Inc.

Author contributions

L.D.G. performed the analysis and led the writing of the paper. H.L.M., S.R.E., D.E.K., F. Muleri and A.D.M. contributed to the IXPE data analysis. I.D., F. Tavecchio, R.W.R., A.P.M. and S.G.J. contributed to the discussion and other parts of the paper, and the latter two provided the VLBA images. I.L. coordinated the multiwavelength observations. I.L. and S.K. contributed the random walk simulations. I.A., C.C., J.E., M.A.G., I. Myserlis, R.R and G.K.K. contributed the radio observations. S.G.J. contributed the infrared observations. S.S.S. performed modelling of the host galaxy in the H band. B.A.-G., F.J.A., I.A., H.A., M.I.B., D.B., G.B., I.G.B., V.C., Y.F., M.G.-C., C.H., R.I., K.S.K., S.K., E.K., P.M.K., E.L., N.M., A. Marchini, T. Mizuno, T.N., S.R., M.S., R.S., A.S., M.U. and A.V. contributed the optical observations. A.A.V. contributed to the paper discussion. R.M., M.P. and S.P. contributed to the Swift data analysis. L.P. and M.N. contributed the Fermi data. The remaining authors are part of the IXPE team whose significant contribution made the X-ray polarization observations possible.

Competing interests

The authors declare no competing interests.

Additional information

Supplementary information The online version contains supplementary material available at https://doi.org/10.1038/s41550-023-02032-7.

Correspondence and requests for materials should be addressed to Laura Di Gesu.

Peer review information *Nature Astronomy* thanks Markus Boettcher and the other, anonymous, reviewer(s) for their contribution to the peer review of this work.

Reprints and permissions information is available at www.nature.com/reprints.

Publisher's note Springer Nature remains neutral with regard to jurisdictional claims in published maps and institutional affiliations.

Springer Nature or its licensor (e.g. a society or other partner) holds exclusive rights to this article under a publishing agreement with the author(s) or other rightsholder(s); author self-archiving of the accepted manuscript version of this article is solely governed by the terms of such publishing agreement and applicable law.

© The Author(s), under exclusive licence to Springer Nature Limited 2023

Laura Di Gesu[1] ✉, Herman L. Marshall[2], Steven R. Ehlert[3], Dawoon E. Kim[4,5,6], Immacolata Donnarumma[1], Fabrizio Tavecchio[7], Ioannis Liodakis[8], Sebastian Kiehlmann[9,10], Iván Agudo[11], Svetlana G. Jorstad[12,13], Fabio Muleri[4], Alan P. Marscher[12], Simonetta Puccetti[14], Riccardo Middei[14,15], Matteo Perri[14,15], Luigi Pacciani[4], Michela Negro[16,17,18], Roger W. Romani[19], Alessandro Di Marco[4], Dmitry Blinov[9,10], Ioakeim G. Bourbah[10], Evangelos Kontopodis[10], Nikos Mandarakas[9,10], Stylianos Romanopoulos[9,10], Raphael Skalidis[9,10,20], Anna Vervelaki[10], Carolina Casadio[9,10], Juan Escudero[11], Ioannis Myserlis[21], Mark A. Gurwell[22], Ramprasad Rao[22], Garrett K. Keating[22], Pouya M. Kouch[8], Elina Lindfors[8], Francisco José Aceituno[11], Maria I. Bernardos[11], Giacomo Bonnoli[7,11], Víctor Casanova[11], Maya García-Comas[11], Beatriz Agís-González[11], César Husillos[11], Alessandro Marchini[23], Alfredo Sota[11], Ryo Imazawa[24], Mahito Sasada[25], Yasushi Fukazawa[24,26,27], Koji S. Kawabata[24,26,27], Makoto Uemura[24,26,27], Tsunefumi Mizuno[26], Tatsuya Nakaoka[26], Hiroshi Akitaya[28], Sergey S. Savchenko[29,30,31], Andrey A. Vasilyev[29], José L. Gómez[11], Lucio A. Antonelli[14,15], Thibault Barnouin[32], Raffaella Bonino[33,34], Elisabetta Cavazzuti[1], Luigi Costamante[1], Chien-Ting Chen[35], Nicolò Cibrario[33,34], Alessandra De Rosa[4], Federico Di Pierro[33], Manel Errando[36], Philip Kaaret[3], Vladimir Karas[37], Henric Krawczynski[36], Lindsey Lisalda[36], Grzegorz Madejski[19], Christian Malacaria[38], Frédéric Marin[32], Andrea Marinucci[1], Francesco Massaro[33,34], Giorgio Matt[39], Ikuyuki Mitsuishi[40], Stephen L. O'Dell[3], Alessandro Paggi[34], Abel L. Peirson[19], Pierre-Olivier Petrucci[41], Brian D. Ramsey[3], Allyn F. Tennant[3], Kinwah Wu[42], Matteo Bachetti[43], Luca Baldini[44,45], Wayne H. Baumgartner[3], Ronaldo Bellazzini[44], Stefano Bianchi[39], Stephen D. Bongiorno[3], Alessandro Brez[44], Niccolò Bucciantini[46,47,48], Fiamma Capitanio[4], Simone Castellano[44], Stefano Ciprini[14,49], Enrico Costa[4], Ettore Del Monte[4], Niccolò Di Lalla[19], Victor Doroshenko[50], Michal Dovčiak[37], Teruaki Enoto[51], Yuri Evangelista[4], Sergio Fabiani[4], Riccardo Ferrazzoli[4], Javier A. Garcia[52], Shuichi Gunji[53], Kiyoshi Hayashida[54], Jeremy Heyl[55], Wataru Iwakiri[56], Fabian Kislat[57], Takao Kitaguchi[51], Jeffery J. Kolodziejczak[3], Fabio La Monaca[4], Luca Latronico[33], Simone Maldera[33], Alberto Manfreda[58], C.-Y. Ng[59], Nicola Omodei[19], Chiara Oppedisano[33], Alessandro Papitto[15], George G. Pavlov[60], Melissa Pesce-Rollins[44], Maura Pilia[43], Andrea Possenti[43], Juri Poutanen[61], John Rankin[4], Ajay Ratheesh[4], Oliver J. Roberts[35], Carmelo Sgrò[44], Patrick Slane[22], Paolo Soffitta[4], Gloria Spandre[44], Douglas A. Swartz[35], Toru Tamagawa[51], Roberto Taverna[62], Yuzuru Tawara[40], Nicholas E. Thomas[3], Francesco Tombesi[6,49,63], Alessio Trois[43], Sergey S. Tsygankov[61], Roberto Turolla[42,62], Jacco Vink[64], Martin C. Weisskopf[3], Fei Xie[4,65] & Silvia Zane[42]

[1]ASI Agenzia Spaziale Italiana, Rome, Italy. [2]MIT Kavli Institute for Astrophysics and Space Research, Massachusetts Institute of Technology, Cambridge, MA, USA. [3]NASA Marshall Space Flight Center, Huntsville, AL, USA. [4]INAF Istituto di Astrofisica e Planetologia Spaziali, Rome, Italy. [5]Dipartimento di Fisica, Università degli Studi di Roma 'La Sapienza', Rome, Italy. [6]Dipartimento di Fisica, Università degli Studi di Roma 'Tor Vergata', Rome, Italy. [7]INAF Osservatorio Astronomico di Brera, Merate, Italy. [8]Finnish Centre for Astronomy with ESO, University of Turku, Turku, Finland. [9]Institute of Astrophysics, Foundation for Research and Technology-Hellas, Heraklion, Greece. [10]Department of Physics, University of Crete, Heraklion, Greece. [11]Instituto de Astrofísica de Andalucía-CSIC, Glorieta de la Astronomía s/n, Granada, Spain. [12]Institute for Astrophysical Research, Boston University, Boston, MA, USA. [13]Department of Astrophysics, St Petersburg State University, St Petersburg, Russia. [14]Space Science Data Center, Agenzia Spaziale Italiana, Rome, Italy. [15]INAF Osservatorio Astronomico di Roma, Rome, Italy. [16]University of Maryland, Baltimore County, Baltimore, MD, USA. [17]NASA Goddard Space Flight Center, Greenbelt, MD, USA. [18]Center for Research and Exploration in Space Science and Technology, NASA/GSFC, Greenbelt, MD, USA. [19]Department of Physics and Kavli Institute for Particle Astrophysics and Cosmology, Stanford University, Stanford, CA, USA. [20]Owens Valley Radio Observatory, California Institute of Technology, Pasadena, CA, USA. [21]Institut de Radioastronomie Millimétrique, Granada, Spain. [22]Center for Astrophysics | Harvard & Smithsonian, Cambridge, MA, USA. [23]University of Siena, Astronomical Observatory, Siena, Italy. [24]Department of Physics, Graduate School of Advanced Science and Engineering, Hiroshima University Kagamiyama, Hiroshima, Japan. [25]Department of Physics, Tokyo Institute of Technology, Tokyo, Japan. [26]Hiroshima Astrophysical Science Center, Hiroshima University, Hiroshima, Japan. [27]Core Research for Energetic Universe (Core-U), Hiroshima University, Hiroshima, Japan. [28]Planetary Exploration Research Center, Chiba Institute of Technology, Narashino, Japan. [29]Astronomical Institute, St Petersburg State University, St Petersburg, Russia. [30]Special Astrophysical Observatory, Russian Academy of Sciences, Nizhnii Arkhyz, Russia. [31]Pulkovo Observatory, St Petersburg, Russia. [32]Université de Strasbourg, CNRS, Observatoire Astronomique de Strasbourg, UMR 7550, Strasbourg, France. [33]Istituto Nazionale di Fisica Nucleare, Sezione di Torino, Turin, Italy. [34]Dipartimento di Fisica, Università degli Studi di Torino, Turin, Italy. [35]Science and Technology Institute, Universities Space Research Association, Huntsville, AL, USA. [36]Physics Department and McDonnell Center for the Space Sciences, Washington University in St Louis, St Louis, MO, USA. [37]Astronomical Institute of the Czech Academy of Sciences, Ondřejov, Czech Republic. [38]International Space Science Institute (ISSI), Bern, Switzerland. [39]Dipartimento di Matematica e Fisica, Università degli Studi Roma Tre, Rome, Italy. [40]Graduate School of Science, Division of Particle and Astrophysical Science, Nagoya University, Nagoya, Japan. [41]Université Grenoble Alpes, CNRS, IPAG, Grenoble, France. [42]Mullard Space Science Laboratory, University College London, Dorking, UK. [43]INAF Osservatorio Astronomico di Cagliari, Selargius, Italy. [44]Istituto Nazionale di Fisica Nucleare, Pisa, Italy. [45]Dipartimento di Fisica, Università di Pisa, Pisa, Italy. [46]INAF Osservatorio Astrofisico di Arcetri, Firenze, Italy. [47]Dipartimento di Fisica e Astronomia, Università degli Studi di Firenze, Sesto Fiorentino, Italy. [48]Istituto Nazionale di Fisica Nucleare, Sezione di Firenze, Sesto Fiorentino, Italy. [49]Istituto Nazionale di Fisica Nucleare, Sezione di Roma 'Tor Vergata', Rome, Italy. [50]Institut für Astronomie und Astrophysik, Universität Tübingen, Tübingen, Germany. [51]RIKEN Cluster for Pioneering Research, Wako, Japan. [52]California Institute of Technology, Pasadena, CA, USA. [53]Yamagata University, Yamagata-shi, Japan. [54]Osaka University, Suita, Japan. [55]University of British Columbia, Vancouver,

British Columbia, Canada. [56]International Center for Hadron Astrophysics, Chiba University, Chiba, Japan. [57]Department of Physics and Astronomy and Space Science Center, University of New Hampshire, Durham, NH, USA. [58]Istituto Nazionale di Fisica Nucleare, Sezione di Napoli, Strada Comunale Cinthia, Naples, Italy. [59]Department of Physics, The University of Hong Kong, Pokfulam, Hong Kong. [60]Department of Astronomy and Astrophysics, Pennsylvania State University, University Park, PA, USA. [61]Department of Physics and Astronomy, University of Turku, Turku, Finland. [62]Dipartimento di Fisica e Astronomia, degli Studi di Padova, Padua, Italy. [63]Department of Astronomy, University of Maryland, College Park, MD, USA. [64]Anton Pannekoek Institute for Astronomy & GRAPPA, University of Amsterdam, Amsterdam, The Netherlands. [65]Guangxi Key Laboratory for Relativistic Astrophysics, School of Physical Science and Technology, Guangxi University, Nanning, China. ✉e-mail: laura.digesu@asi.it